Supplementary Information

Immunomimetic Bioengineered Vesicles Targeting TGF-β and PD-L1 Enhance Antitumor Efficacy through Pyroptosis-Driven Trained Immunity Coordinated with Adaptive Immunity

*Peng Zheng[1,4], Sihang Bao[1,2,4], Tong Yu[1,4], Ying Yang[1], Xin Yin[1], Yu Liu[1], Yiru Tian[1], Xiang Zhang[1,3], Shuqin Li[1], Qiong Long[1], Hongmei Bai[1], Xu Yang[1], Yanbing Ma[1,2,3]**

[1]Laboratory of Molecular Immunology, Institute of Medical Biology, Chinese Academy of Medical Sciences & Peking Union Medical College, Kunming 650118, China
[2]School of Life Sciences, Yunnan University, Kunming 650091, China
[3]Kunming Medical University, Kunming 650500, China
[4]These authors contributed equally: Peng Zheng, Sihang Bao, Tong Yu.
* Correspondence: MolecularImmunology@imbcams.com.cn

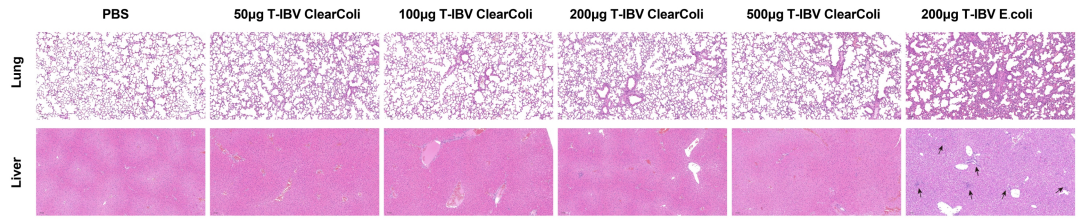

Figure S1. Representative H&E-stained images of the lungs and liver. 72 hours after a single intravenous injection of T-IBV derived from *ClearColi* at various indicated doses (50 μg, 100 μg, 200 μg, 500 μg) and 200 μg of *E. coli* T-IBV, the lungs and livers were harvested for H&E staining analysis;the black arrows indicate infiltrating immune cells.

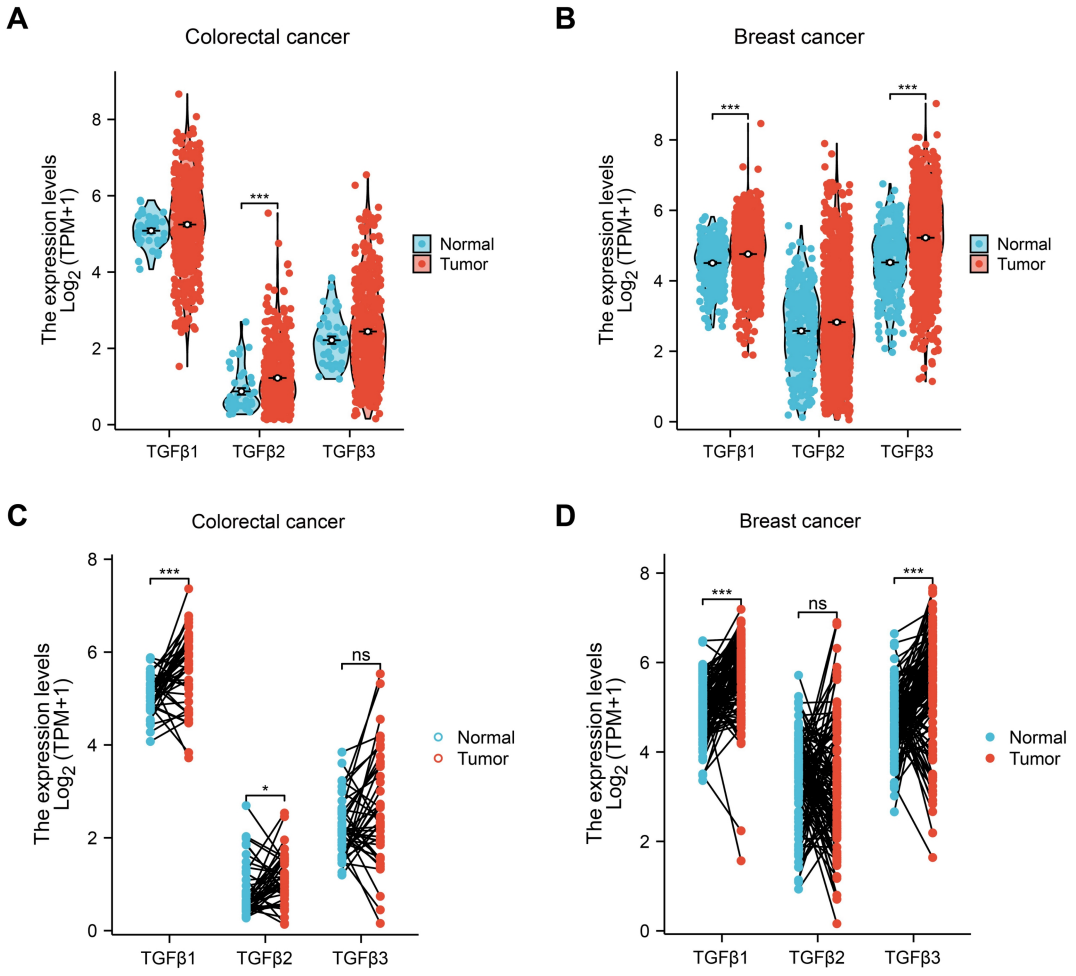

Figure S2. Analysis of the expression of different TGFβ subtypes in clinical cancer patients. (A) RNA-seq data from the TCGA-COAD (colon cancer) project's STAR workflow were downloaded from the TCGA database, organized, and extracted in TPM format. (B) TPM-formatted RNA-seq data from TCGA and GTEx were uniformly processed via the Toil workflow on UCSC XENA. Data corresponding to BRCA (invasive breast cancer) from TCGA and corresponding normal tissue data from GTEx were extracted. (C) RNA-seq data from the STAR workflows of the TCGA-COAD (C) and TCGA-BRCA (D) projects were downloaded from the TCGA database, organized, and extracted in TPM format. We extracted paired normal and tumor samples with corresponding identifiers for analysis. In colorectal cancer, the statistical sample sizes for TGFβ1, TGFβ2, and TGFβ3 were 326, 414, and 528 cases, respectively. In breast cancer, the sample sizes for TGFβ1, TGFβ2, and TGFβ3 were 886, 3,848, and 1,426 cases, respectively. Statistical significance was determined using the Wilcoxon rank-sum test (A–D).

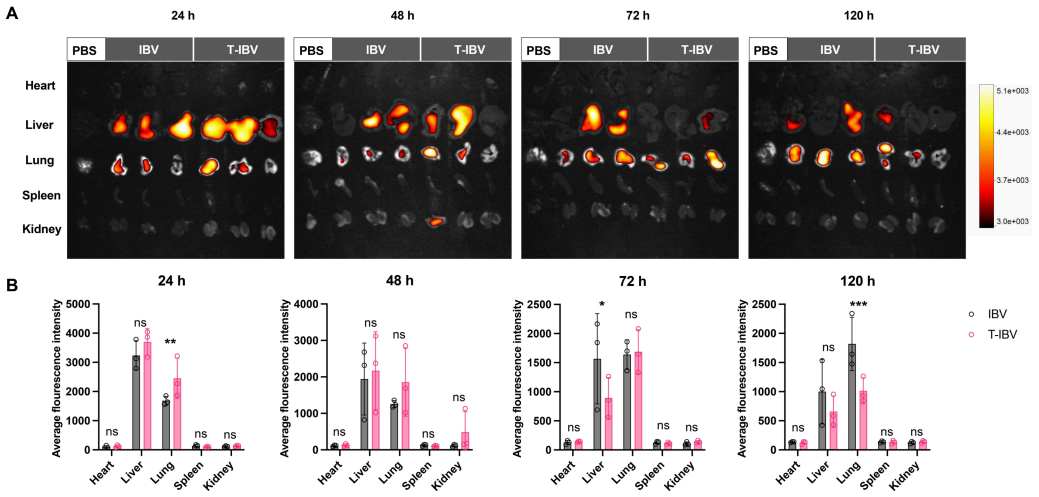

Figure S3. Dynamic distribution of T-IBV in major organs of mice following intravenous injection. (A) Fluorescence images of mouse organs at different time points; (B) Statistical plots of fluorescence intensity at different time points. (A) Changes in ex vivo fluorescence imaging of major organs in MC38 tumor-bearing mice at different time points (24 h, 48 h, 72 h, 120 h) following injection of Dil-labeled T-IBV; (B) Statistics on changes in fluorescence intensity in different organ tissues at different time points (n = 3); Dil-labeled IBV served as a control. Data are shown as the mean ± standard deviation (SD). Statistical significance was determined using two-way ANOVA (B). *p < 0.05, **p < 0.01, ***p < 0.001, ****p < 0.0001; ns, not significant.

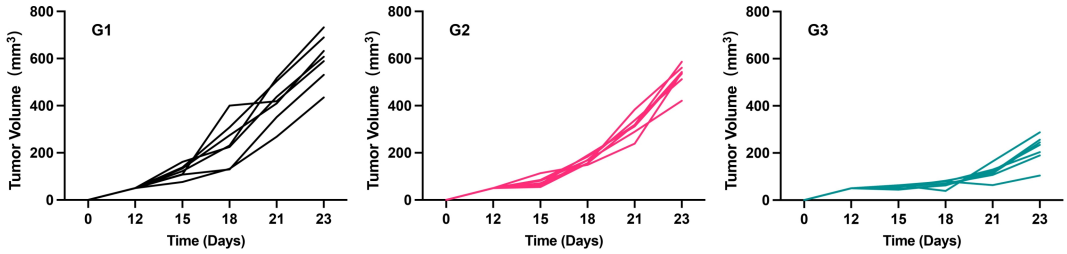

Figure S4. Individual tumor growth curves for mice in different treatment groups (corresponding to Figure 4B). G1: PBS; G2: IBV; G3: T-IBV.

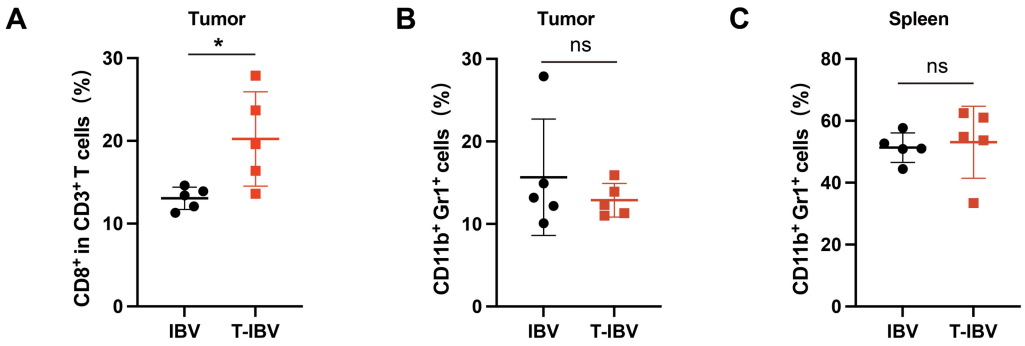

Figure S5. Analysis of immune cells following T-IBV treatment in 4T1 tumor-bearing mice. (A) Flow cytometric analysis of the proportion of infiltrating CD8 T cells ($CD3^+CD8^+$) in tumors (n=5); (B) Flow cytometric analysis of the proportion of MDSCs ($CD11b^+Gr\text{-}1^+$) in tumors (n=5); (C) Flow cytometric analysis of the proportion of MDSCs ($CD11b^+Gr\text{-}1^+$) in the spleen (n=5). Data are shown as the mean ± standard deviation (SD). Statistical significance was determined using unpaired two-tailed Student's t-tests (A – C). *$p < 0.05$, **$p < 0.01$, ***$p < 0.001$, ****$p < 0.0001$; ns, not significant.

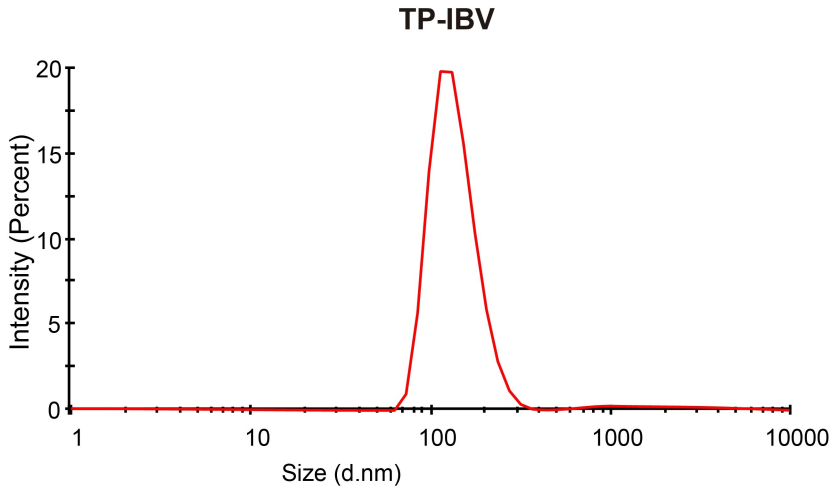

Figure S6. Particle size distribution characteristics of TP-IBV as determined by DLS (corresponding to Figure 5P).

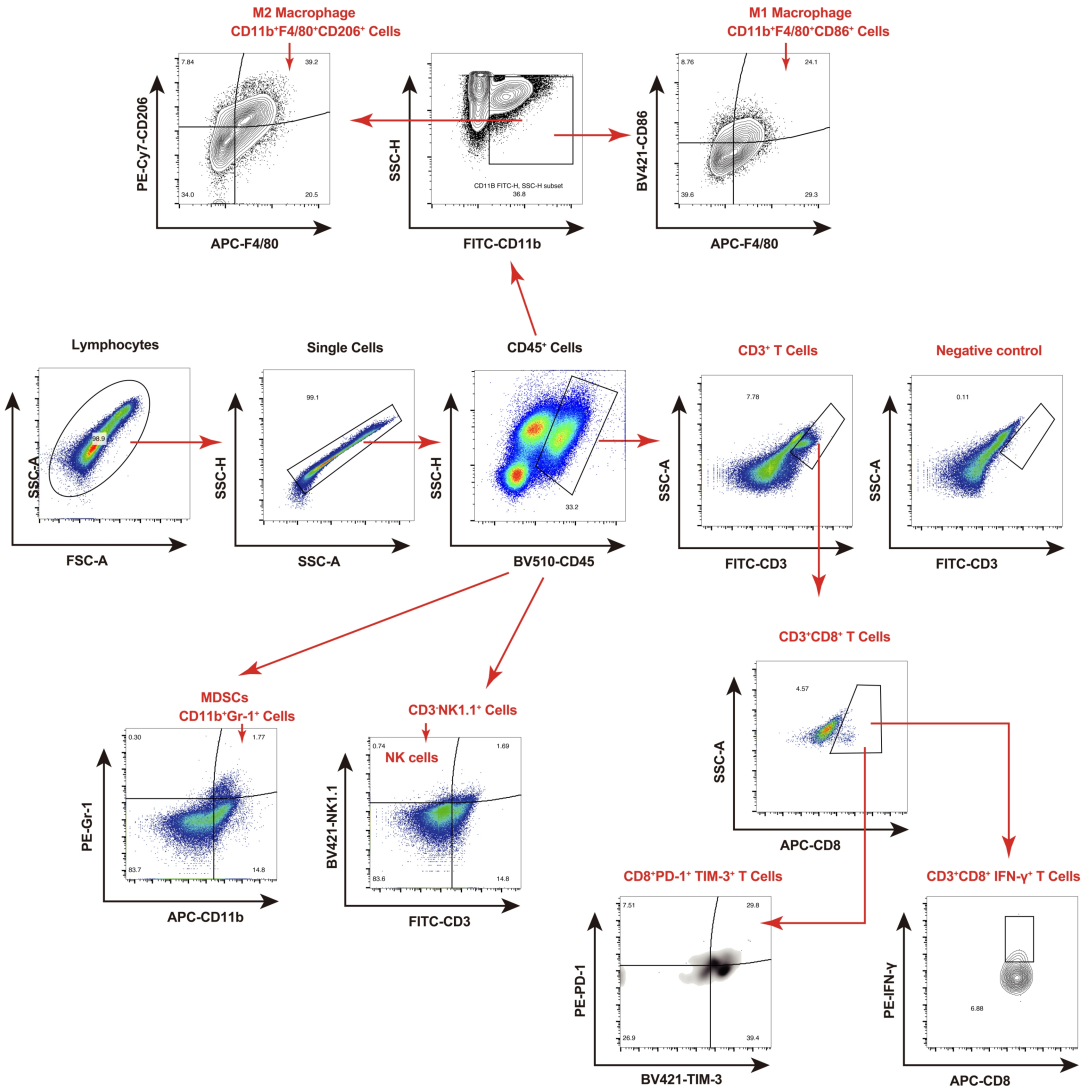

Figure S7. Gating strategies for different types of immune cells in tumors using flow cytometry. FSC-A, forward scatter area; SSC-A, side scatter area; SSC-H, side scatter height.

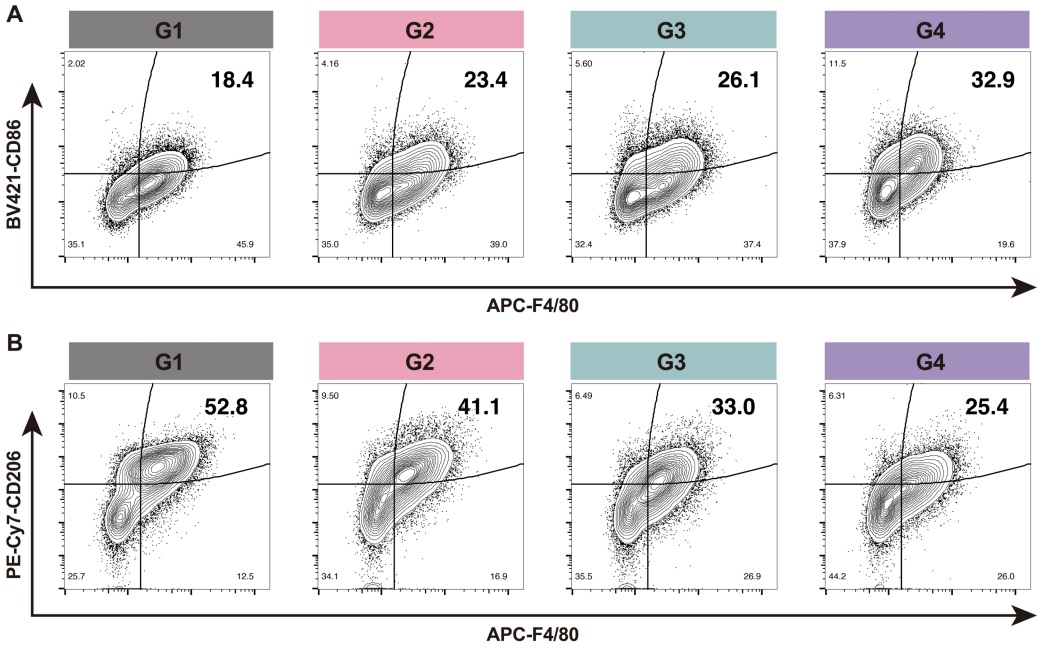

Figure S8. Representative flow cytometry plots showing the proportion of tumor-associated macrophages (TAMs) in tumor tissues from different treatment groups. (A) Representative flow cytometry plot showing the proportion of M1 TAMs ($CD11b^+F4/80^+CD86^+$) in tumors (corresponding to Figure 6A); (B) Representative flow cytometry plot showing the proportion of M2 TAMs ($CD11b^+F4/80^+CD206^+$) in tumors (corresponding to Figure 6B).

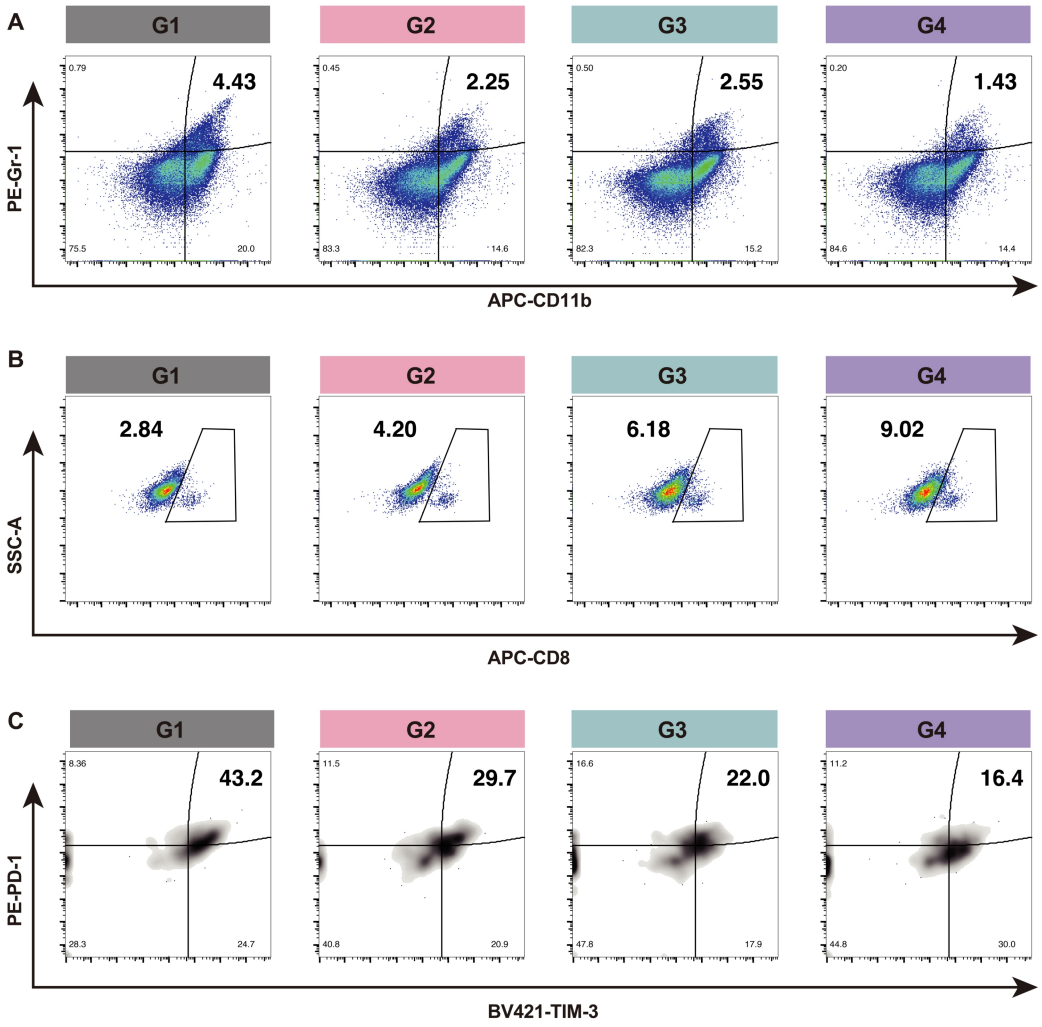

Figure S9. Representative flow cytometry plots showing the proportion of immune cells in tumor tissue across different treatment groups. (A) Representative flow cytometry plot showing the proportion of MDSCs ($CD11b^{+}Gr\text{-}1^{+}$) in tumors (corresponding to Figure 6D); (B) Representative flow cytometry plot showing the proportion of CD8 T cells ($CD3^{+}CD8^{+}$) in tumors (corresponding to Figure 6E); (C) Representative flow cytometry plot showing the proportion of exhausted T cells ($CD8^{+}PD\text{-}1^{+}TIM\text{-}3^{+}$) in tumors (corresponding to Figure 6F).

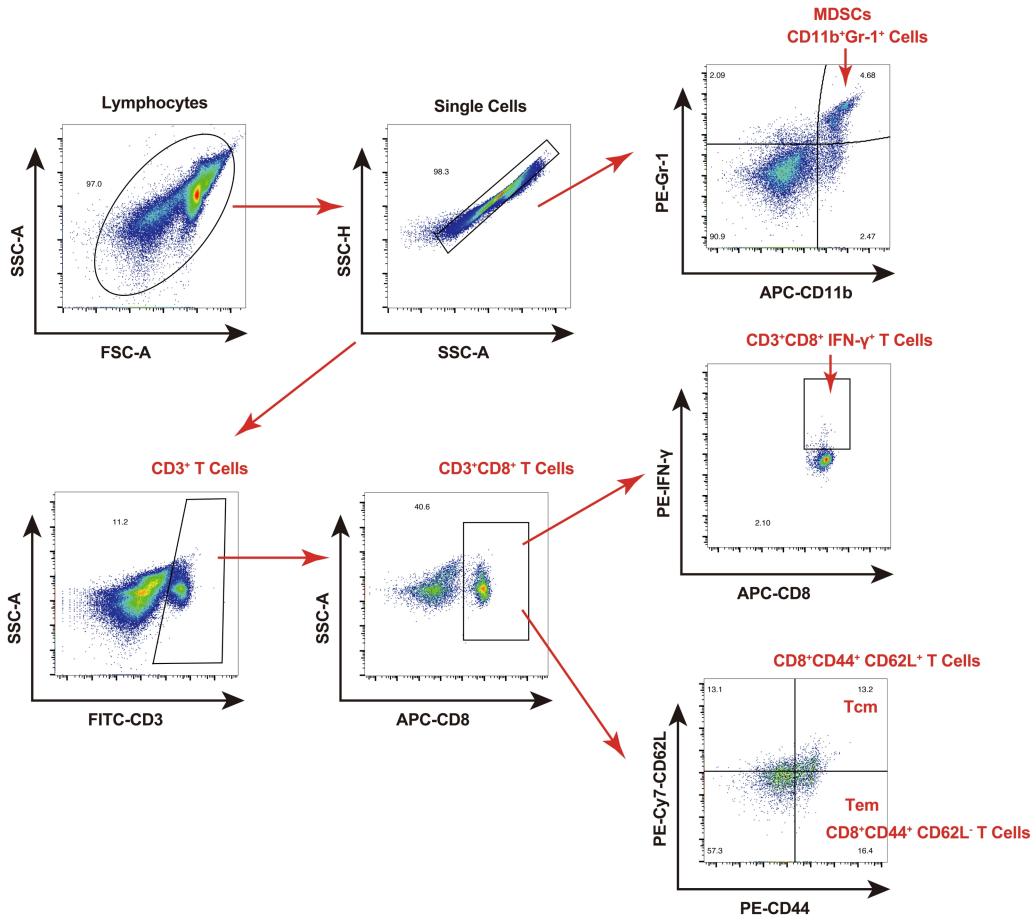

Figure S10. Gating strategy for different types of immune cells in the spleen using flow cytometry. FSC-A, forward scatter area; SSC-A, side scatter area; SSC-H, side scatter height.

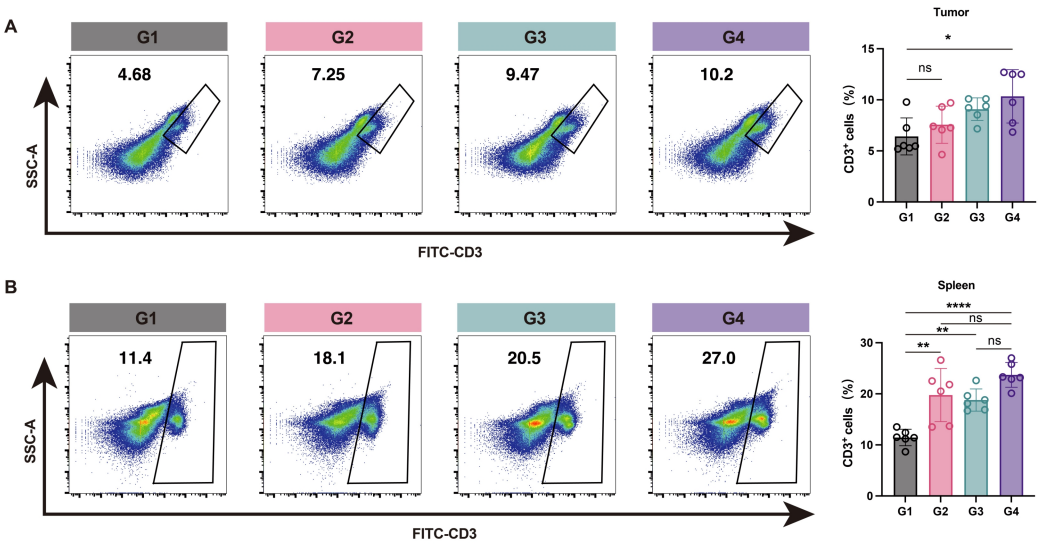

Figure S11. Representative flow cytometry plots and statistical analysis of CD3 T-cell proportions in tumors and the spleen. (A) Representative flow cytometry plots and statistical analysis of CD3 T-cell proportions in tumors from different treatment groups (n = 6); (B) Representative flow cytometry plots and statistical analysis of CD3 T-cell proportions in the spleen from different treatment groups (n = 6). Data are shown as the mean ± standard deviation (SD). Statistical significance was determined using one-way analysis of variance (ANOVA) followed by Tukey's multiple comparisons (A, B). *p < 0.05, **p < 0.01, ***p < 0.001, ****p < 0.0001; ns, not significant.

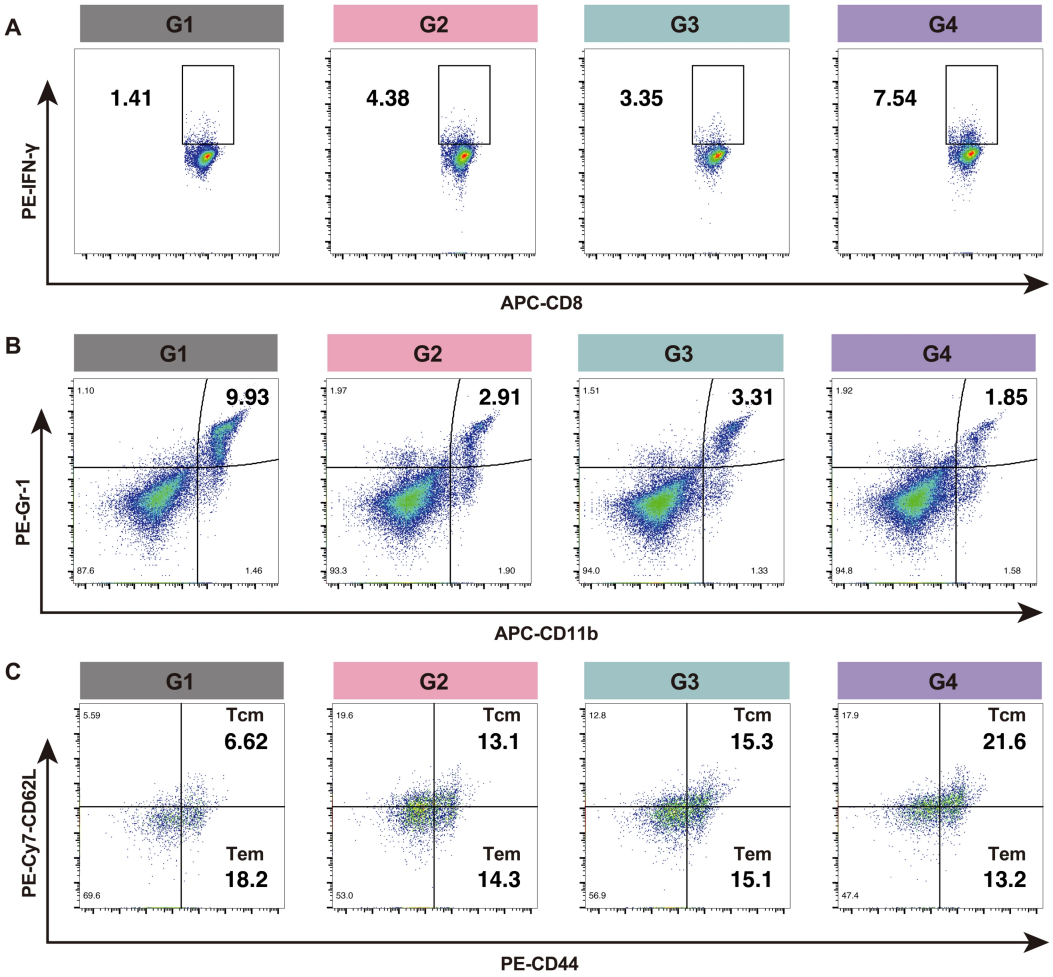

Figure S12. Representative flow cytometry plots showing immune cell proportions in the spleen of the designated treatment groups. (A) Representative flow cytometry plot showing the proportion of Adpgk-specific CTL cells ($CD3^+CD8^+IFN\text{-}\gamma^+$) in the spleen (corresponding to Figure 6N); (B) Representative flow cytometry plot showing the proportion of MDSCs ($CD11b^+Gr\text{-}1^+$) in the spleen (corresponding to Figure 6O); (C) Representative flow cytometry plot showing the proportion of CD8 central memory T cells (Tcm) ($CD8^+CD44^+CD62L^+$) in the spleen (corresponding to Figure 6P).

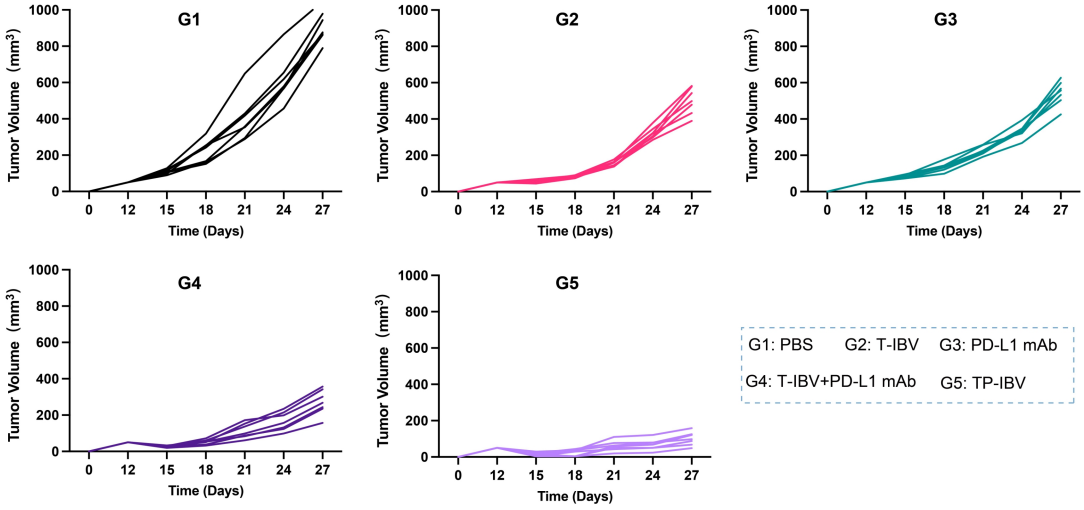

Figure S13. Individual tumor growth curves after treatment in different indicated experimental groups (corresponding to Figure 7B).

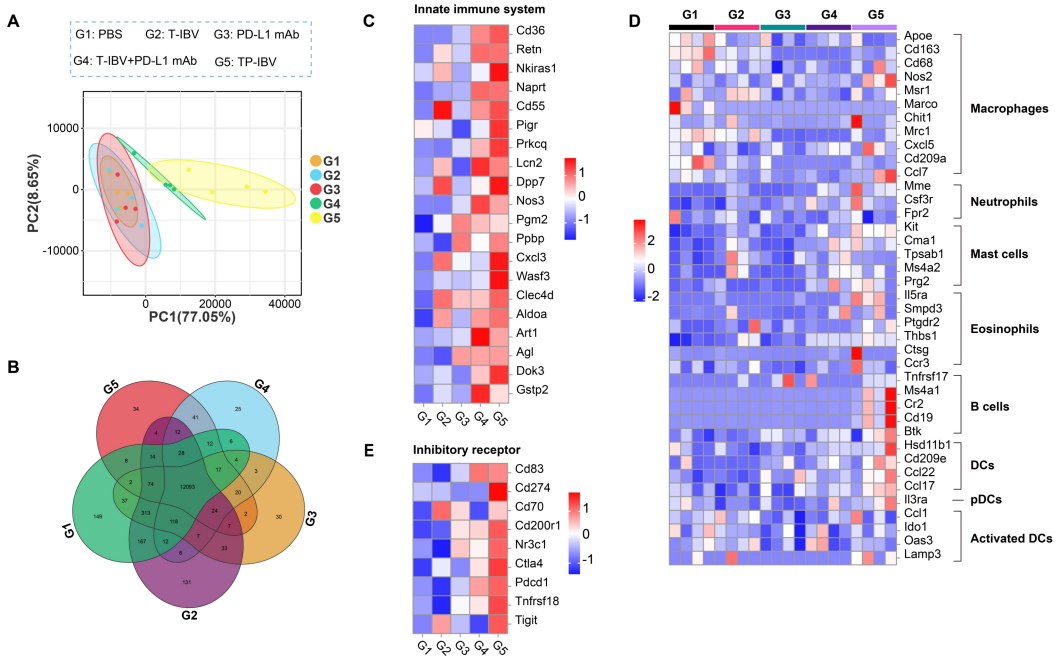

Figure S14. Analysis of RNA-Seq data on TP-IBV-induced TME remodeling in cold tumors. (A) Principal component analysis (PCA) plot of sequenced samples from different experimental groups (n=4). (B) Venn diagram showing changes in gene regulation after treatment in different experimental groups; (C) RNA-Seq heatmap showing the expression of genes associated with the innate immune system in tumor tissues from mice treated with PBS, T-IBV, PD-L1 mAb, T-IBV+PD-L1 mAb, and TP-IBV. (D) Heatmaps showing the expression of genes associated with different immune cell types in tumor tissues from mice in each designated treatment group. Data for each gene are presented as z-scores of gene expression values normalized to the PBS group (n = 4). (E) Heatmap of RNA-seq data showing the expression of genes associated with inhibitory receptors in tumor tissues from mice treated with PBS, T-IBV, PD-L1 mAb, T-IBV+PD-L1 mAb, and TP-IBV.

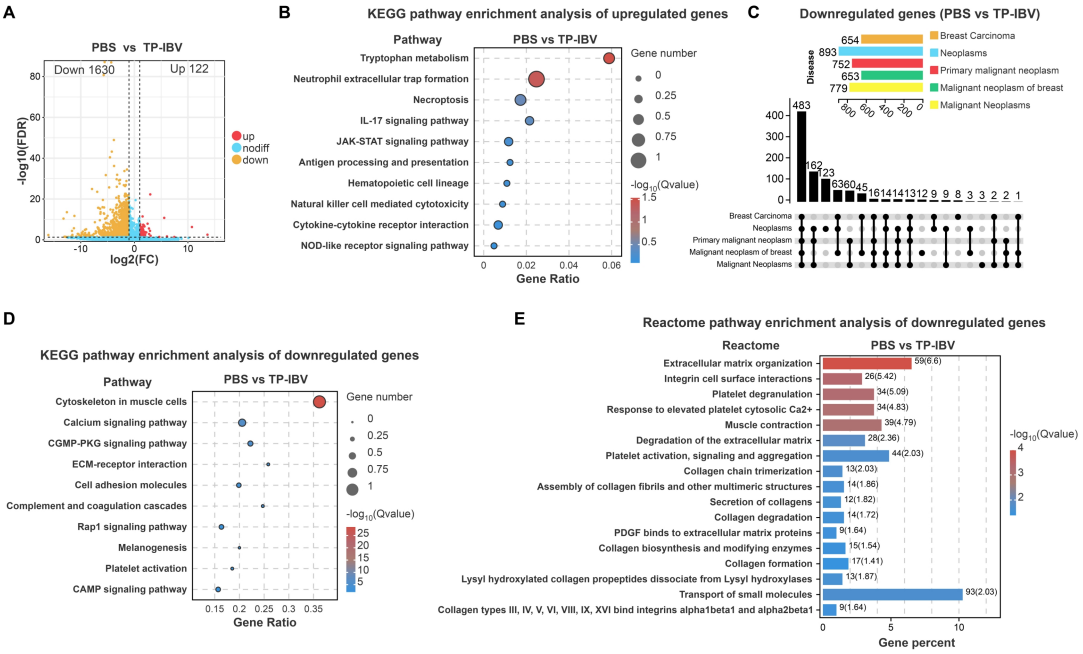

Figure S15. Enrichment analysis of gene pathways up- and down-regulated by TP-IBV. (A) Volcano plot of genes up- and down-regulated by TP-IBV compared to PBS; (B) KEGG pathway enrichment analysis of genes up-regulated by TP-IBV. (C) DisGeNET disease enrichment analysis of downregulated genes; (D) KEGG pathway enrichment analysis of TP-IBV-downregulated genes; (E) Reactome pathway enrichment analysis of TP-IBV-downregulated genes.

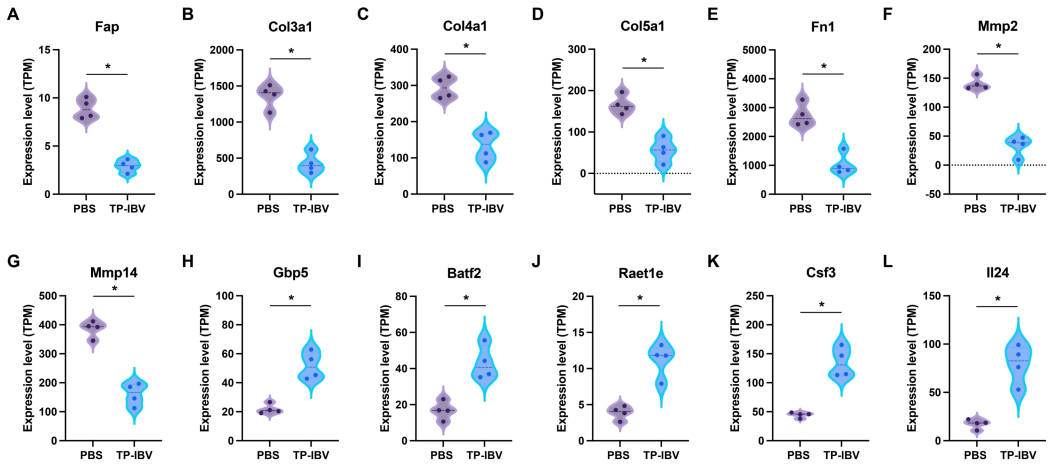

Figure S16. Transcriptomic analysis of TP-IBV effects on gene expression related to tumor stromal remodeling, fibroblast activation, collagen formation, and innate immune activation. (A) Expression levels of Fap, a key marker of cancer-associated fibroblast (CAF) activation; (B–D) Genes encoding major collagens (Col3a1, Col4a1, Col5a1); (E–G) Expression of genes encoding key enzymes and related proteins (Fn1, Mmp2, Mmp14) that regulate extracellular matrix (ECM) metabolism, remodeling, and invasive capacity; (H) Expression of the interferon-induced GTPase Gbp5; (I) Expression of Batf2, a key transcription factor for dendritic cell (DC) activation; (J) Expression of Raet1e, an important ligand for activating NK cells and T cells; (K) Expression of Csf3, a gene associated with myeloid cell mobilization; (L) Expression of Il24, an important gene with pro-tumor cell apoptosis effects.

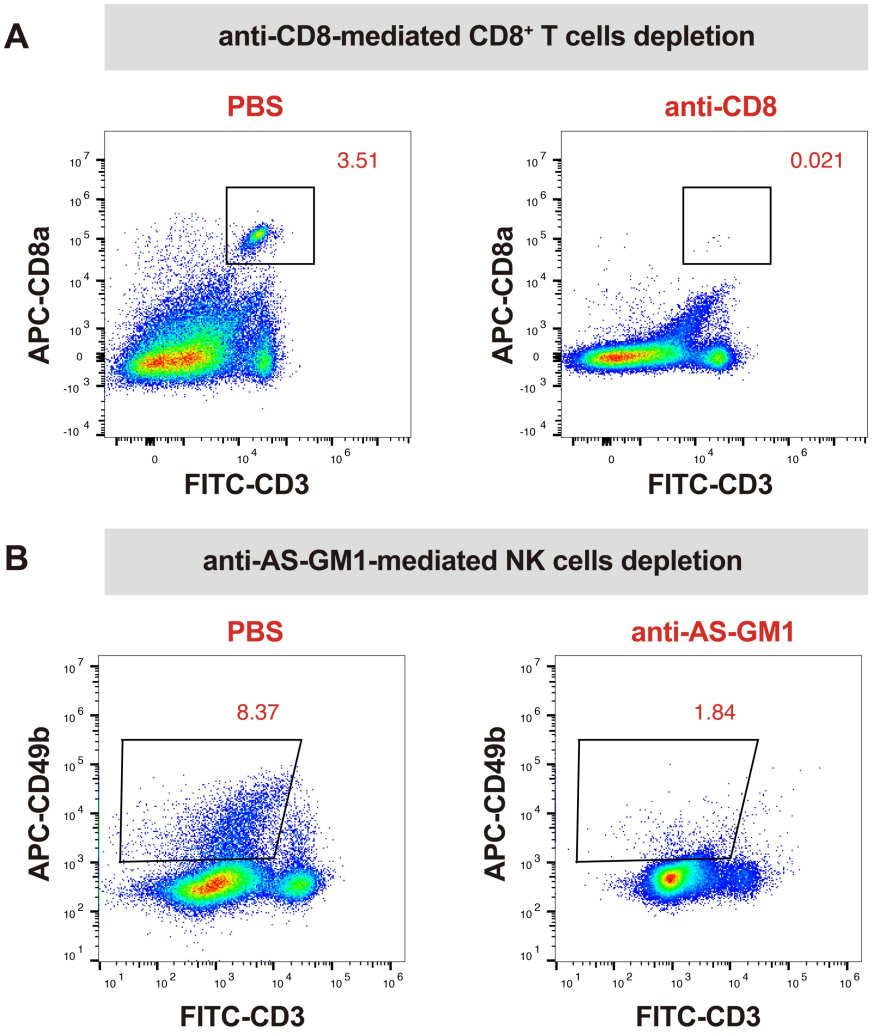

Figure S17. Validation of antibody-mediated depletion of CD8 T cells and NK cells. (A) Representative flow cytometry scatter plot showing CD8 T cells in the spleen of 4T1-tumor-bearing mice following anti-CD8 mAb-mediated depletion; (B) Representative flow cytometry scatter plot showing NK cells in the spleen of 4T1-tumor-bearing mice following anti-AS-GM1 mAb-mediated depletion.